



Enriching Trace Level Adsorption Affinity of As^{3+} Ion Using Hydrothermally Synthesized Iron-Doped Hydroxyapatite Nanorods

Sandeep Eswaran Panchu¹ · Saranya Sekar¹ · Vani Rajaram² · Elayaraja Kolanthai³ · Sarojini Jeeva Panchu⁴ · Hendrik C. Swart⁴ · S. Narayana Kalkura¹

Received: 16 June 2021 / Accepted: 7 September 2021 / Published online: 16 September 2021
© The Author(s), under exclusive licence to Springer Science+Business Media, LLC, part of Springer Nature 2021

Abstract

Contamination of arsenic in the form of arsenite (As^{3+}) and arsenate (As^{5+}) in potable water causes serious illness in the human body even at a very low concentration ($10 \mu\text{g/L}$). As^{3+} is comparatively 60 times more toxic than As^{5+} species. This work is focused on the preparation of adsorbents for efficient removal of As^{3+} with higher adsorption affinity at trace level ($\leq 50 \mu\text{g/L}$). The iron-doped hydroxyapatite (Fe-HAp) synthesized by hydrothermal technique is employed as an efficient adsorbent. A significantly less quantity of Fe^{2+} ion (0.5 wt%) is incorporated in the tetrahedral and octahedral sites of the HAp lattice along the *c*-axis, which leads to a drastic reduction in particle size (400% in length and 225% in width) and enhances the specific surface area (105%), colloidal stability, and adsorption affinity. The maximum adsorption capacity of As^{3+} is $139 \pm 2 \mu\text{g/g}$ and $183 \pm 2 \mu\text{g/g}$ for HAp and Fe-HAp, respectively. The adsorption rate of Fe-HAp is very rapid, which is 538% higher than HAp. Also, the As^{3+} adsorption affinity or sensitivity ($0.71 \mu\text{g/L}$) significantly improved 83–99% when compared to the adsorbents reported in the previous literature. The adsorption capacity of As^{3+} ion was unaffected by other competing ions and obtained 97% recycling efficiency up to 7 cycles using Fe-HAp. The monolayer adsorption of As^{3+} is purely strong chemisorption as confirmed by the Langmuir and Dubinin–Radushkevich (DKR) isotherm. The structure and morphology of HAp and Fe-HAp remain unchanged after the adsorption of As^{3+} ions and also no secondary toxic products were observed. Hence, the above results reveal Fe-HAp as an efficient and low-cost adsorbent for the removal of highly toxic As^{3+} ions at the trace level.

✉ S. Narayana Kalkura
kalkura@gmail.com

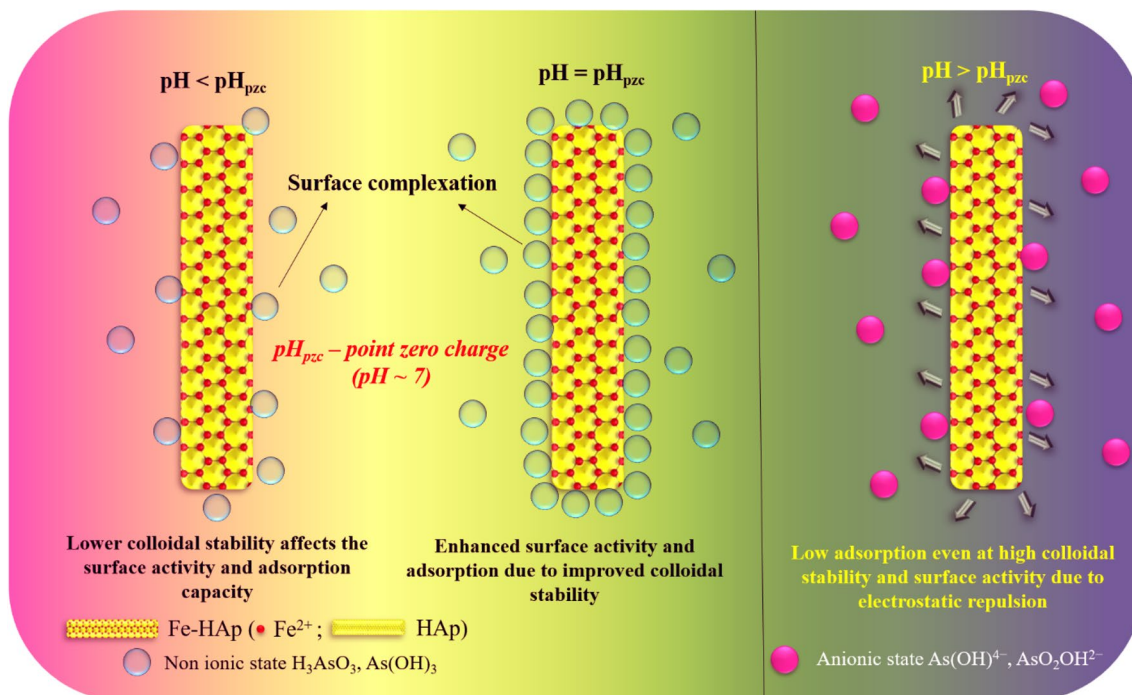
¹ Crystal Growth Centre, Anna University, Chennai,
Tamil Nadu 600025, India

² Meenakshi College for Women, Kodambakkam, Chennai,
Tamil Nadu 600024, India

³ Department of Materials Science & Engineering, Advanced
Materials Processing and Analysis Center, University
of Central Florida, Orlando, FL, USA

⁴ Department of Physics, University of the Free State, PO
Box 339, Bloemfontein 9300, South Africa

Graphic Abstract



Keywords Hydrothermal · Colloidal stability · Surface charge · Surface complexation · As^{3+} adsorption · Adsorption isotherm

1 Introduction

Arsenic (As) is a familiar toxic metal ion found in groundwater as a contaminant. The World Health Organization (WHO) recommended that the limit of As in drinking water is $\leq 10 \mu\text{g/L}$. However, more than 60 million people are said to be affected by As contamination, which is exceeding WHO limits [1–5]. Consumption of As contaminated water causes carcinogenic effects in the skin, urinary bladder, liver, kidney, and lung [6–9]. Generally, As has four different chemical forms in an aquatic environment based on the oxidation state -3 , 0 , $+3$, and $+5$. The existence of As in 0 and -3 oxidation states in water is extremely rare. In contrast, $+3$ and $+5$ states are prominently found in the natural water source, which depends on the redox reaction and pH condition [10, 11]. In groundwater, As^{3+} is found in neutral species such as $As(OH)_3$, H_3AsO_3 , $As(OH)_4^-$, AsO_2OH^{2-} , and AsO_3^{3-} , whereas As^{5+} is found in anionic forms such as AsO_4^{3-} or $H_2AsO_4^-$ or $HAsO_4^{2-}$ [12, 13]. In comparison, the prevalence of As^{3+} contaminated groundwater is approximately 67–99% higher than As^{5+} ions and the toxicity rate of As^{3+} is 60 times greater than the As^{5+} [14]. In addition, As^{3+} shows less adsorption affinity than As^{5+} because As^{3+} is a neutral compound, whereas As^{5+} is an anionic compound.

The anionic compound has improved the attractive force between the adsorbent and adsorbate ions [7].

Various technologies have been applied to remove arsenic from contaminated water, such as chemical precipitation, flocculation, ion exchange and reverse osmosis [9, 12, 13]. But, these technologies have limitations when implementing into large-scale processes. The membrane technology, a reverse osmosis process, requires high electric power and skilled technicians to operate. Likewise, the flocculation, ion exchange, and precipitation methods are problematic due to their complexities in disposing of secondary products [13]. Recently, the adsorption technique has emerged as an effective alternative method because it is a simple and cost-effective method for removing arsenic [15–17]. A variety of adsorbents were employed to remove As from water. Generally, calcium phosphate (CaP) based adsorbent HAp [$Ca_{10}(PO_4)_6(OH)_2$] has been widely used to remove arsenic from water. This may be due to the fact that HAp is highly biocompatible, porous in nature, relatively inexpensive, easy to modify the structural and morphological characteristics based on synthesis routes, and ensures safe drinking water [18]. Furthermore, nano-sized adsorbents were used to remove the metal ions due to their high surface area, adsorption capacity, and affinity. They are iron-oxide-coated

quartz (IOCQ), biochar, magnetic Fe-hydroxalcalite, activated alumina, sulfate-modified iron oxide-coated sand, iron oxide-coated sand, 6%Cu-HAp3, HAp from fish scale, and $\text{Fe}_2\text{O}_3\text{-ZrO}_2\text{/BC}$ [19–27]. Li et al., reported the Fe^{3+} doped HAp with enhanced dispersion stability via highly effective removal of tetracycline than pure HAp [28]. Mercado et al., reported that the surface and morphological modification of magnetic iron-doped HAp nanoparticle increase the adsorption capacity of Cu^{2+} ion than Pure HAp nanoparticles [29]. Saber-Samandari et al., reported that the chitosan/Fe-substituted hydroxyapatite composite beads exhibit significant enhancement of Pb^{2+} and methylene blue adsorption capacity [30]. Similarly, Xiao et al., reported magnetic $\gamma\text{-Fe}_2\text{O}_3\text{/Fe}$ -doped hydroxyapatite nanostructures for removing Cd^{2+} ions [31].

Even though HAp has been employed to absorb a wide variety of metal ions such as Cr, Co, Cd, Pb, and As, still HAp lacks adsorption affinity towards arsenic ions. This paper elucidates the mechanism of incorporating Fe^{2+} ions into the HAp lattice to improve the arsenic adsorption affinity and adsorption capacity. [32–35]. To the best of our knowledge, the present work is the first report on removing the As^{3+} ion using Fe doped HAp. The geometry of Fe^{2+} ion incorporated in the HAp lattice results in the charge neutralization process, thereby enhancing the colloidal stability of HAp. The incorporated Fe^{2+} ion interacts with oxygen vacancy of phosphate ion leading to the formation of Fe–O–OH. This formation reduced the oxygen vacancy and thereby decreasing the crystallite size and particle size of HAp. In addition, the formation of Fe–O–OH functional groups improves the adsorption affinity and adsorption capacity of As^{3+} ions [2, 36].

The removal of highly toxic As^{3+} ion at trace level using hydrothermally synthesized nano-sized Fe-HAp was employed as an adsorbent to overcome the problem mentioned above. The schematic representation of incorporating the Fe^{2+} ion which improves the adsorbent characteristic features, is as shown in Fig. 1. Also, this work elucidates the importance of colloidal stability and zero-point charge of the adsorbent. The maximum adsorption capacity was found by the batch adsorption process. The nature of the adsorption process was discussed using Langmuir, Freundlich, and DKR isotherm. Ultimately, this work aims to enhance trace level adsorption affinity, As^{3+} adsorption capacity and maintain the water quality.

2 Experimental Section

2.1 Materials and Methods

The chemicals used in this experimental study are Calcium nitrate tetrahydrate ($\text{Ca}(\text{NO}_3)_2 \cdot 4\text{H}_2\text{O}$), diammonium

hydrogen orthophosphate ($(\text{NH}_4)_2\text{HPO}_4$), Iron (II) chloride (FeCl_2), Hydrochloric acid (HCl), Ammonia solution (NH_4OH), and Sodium arsenite (NaAsO_2). All the chemicals were purchased from Merck analytical grade. Triple distilled water was used to prepare adsorbent and adsorbate ions.

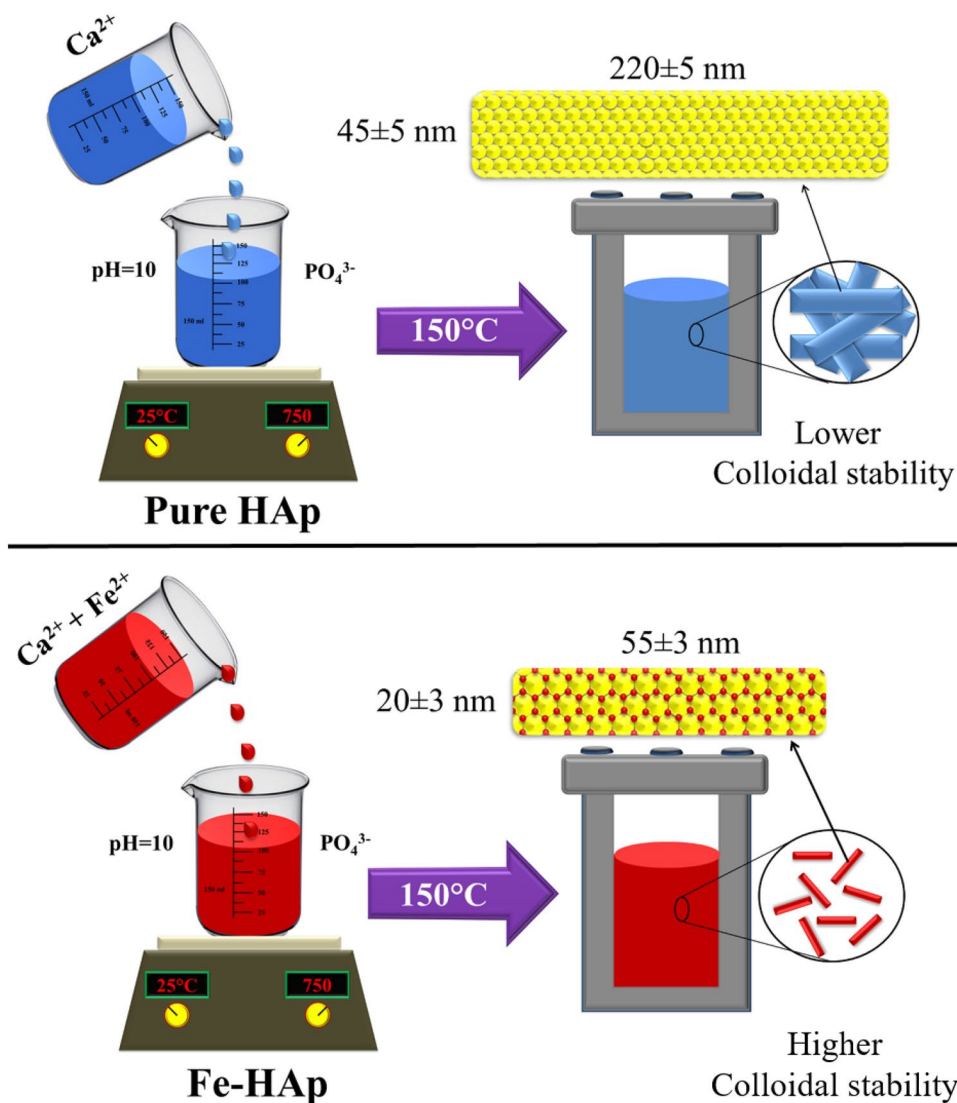
2.2 Synthesis of HAp and Fe-HAp

1 M of calcium nitrate tetrahydrate and 0.6 M of diammonium hydrogen orthophosphate were dissolved in 100 mL of triple distilled water in separate beakers. 1 M of calcium nitrate tetrahydrate was added drop-wise into 0.6 M of diammonium hydrogen orthophosphate by maintaining the pH of the product solution at 10 using ammonia to synthesize HAp. The obtained precipitated solution was continuously stirred for 2 h and transferred into a 100 mL Teflon-lined stainless-steel autoclave and kept in an oven at 150 °C for 36 h. Subsequently, the autoclave was allowed to reach room temperature and the solution was centrifuged with triple distilled water to remove the unreacted ammonia from the precipitated HAp. Finally, the collected precipitates were dried in a vacuum oven at 80 °C for 24 h. The Fe-HAp was synthesized by mixing 0.1 M of ferric chloride with 1 M of calcium nitrate tetrahydrate. The rest of the synthesis procedure is the same as the preparation of HAp described above.

2.3 Characterizations

Powder X-ray diffraction (XRD) of the synthesized adsorbent was recorded by Rigaku Ultima IV X-ray diffractometer equipped with monochromatic Cu K_α radiation ($\lambda = 0.154 \text{ nm}$) in the 2θ range of 10° to 70° with scanning step size of 0.02°. The functional group of the adsorbent was analyzed by Fourier transform infrared spectrometer (FT-IR-JASCO-6300) using the KBr pellet technique. The adsorbent morphology was analyzed using High-resolution transmission electron microscopy (HRTEM, JEOL Japan, JEM-2100 Plus) and High-resolution scanning electron microscopy (HRSEM, F E I Quanta FEG 200). The specific surface area, pore size, and pore volume of the adsorbent material were measured by Brunauer–Emmett–Teller (BET) isotherm model by using surface area analyzer-TPD/TPR (Model: Quanta chrome). The adsorbent zeta potential was measured by Dynamic Light Scattering (DLS-Malvern Zetasizer Nano-ZS). The removal capacity of As^{3+} was evaluated by utilizing an Atomic Absorbance spectrometer (AAS-ICE 33-00 from Thermo fisher) equipped with a hydrate generator. Material composition for before and after adsorption of As^{3+} was analyzed by ICP-OES (Perkin Elmer Optima 5300 DV). The pH of the solution was measured by using a Eutech pH meter with a sensitivity of 0.01.

Fig. 1 Schematic representation of tailoring ability of incorporated Fe^{2+} ion and enhances physicochemical properties of the adsorbent



2.4 Batch Adsorption Study

1000 $\mu\text{g/L}$ of As^{3+} stock solution was prepared from sodium arsenite as a precursor material. The required concentrations were obtained by the dilution of stock solution using triple distilled water. Initially, 100 mg of adsorbents were added to 20 ml of 1000 $\mu\text{g/L}$ of As^{3+} solution that was used to investigate the effect of contact time (0 to 50 min). The rest of the parameters pH (7), rpm (180), and temperature (25 ± 1 °C) were kept constant. After that, the evaluated contact time (10 min) was fixed to subsequent studies on the concentration effect of As^{3+} (100 $\mu\text{g/L}$ to 1000 $\mu\text{g/L}$), and the rest of the adsorption parameters were kept constant. The maximum removal capacity of As^{3+} is measured from Eq. (1). All the experiments were conducted in triplicate with an error percentage of $\pm 1\%$. After adsorption of As^{3+} , HAp and Fe-HAp were named as HAp-As and Fe-HAp-As.

$$\text{Adsorption capacity}(Q_e) = (C_o - C_f) \times \left(\frac{V}{M}\right) \quad (1)$$

where Q_e is the equilibrium adsorption capacity ($\mu\text{g/g}$). C_o and C_f are the initial and final concentrations of adsorbate solution ($\mu\text{g/L}$). V and M are the volumes of the solution (mL) and mass of the adsorbent dosage (mg), respectively [29, 37–39].

2.5 Quantification of Fe^{2+} Ion

The presence of doping iron in HAp was estimated by dissolving 10 mg of Fe-HAp in 20 ml of HCl (0.1 M) solution. Furthermore, the concentration of Fe^{2+} ion released in triple distilled water and As^{3+} contaminated water was calculated by the following procedure. 100 mg of Fe-HAp was soaked in 20 mL of triple distilled water and As^{3+} contaminated water (pH=7; shaking speed=180 rpm) at room

temperature. After the equilibrium time (10 min), the supernatant solution was tested in AAS.

3 Results and Discussion

3.1 X-ray Diffraction Analysis

The XRD patterns of the HAp, Fe-HAp, HAp-As and Fe-HAp-As are shown in Fig. 2a. The diffraction pattern of as-synthesized HAp and Fe-HAp exhibited crystalline nature, and matched well with the characteristic peaks of HAp phase

(JCPDS card No. 09-0432) [40, 41]. The absence of any significant shift in the diffraction peak of Fe-HAp towards the higher angle confirms that the Ca^{2+} ion was not substituted by the Fe^{2+} ions [29, 42–44]. In HAp, the a -axis is positively charged due to the presence of Ca^{2+} ions. In contrast, the c -axis is negatively charged due to the influence of phosphate and hydroxide ions, which enables the incorporation of cationic Fe^{2+} ions as shown in the schematic representation of Fig. 2b [45, 46]. Hence, the doped Fe^{2+} ions were expected to be incorporated in the interstitial position either at the tetrahedral or octahedral vacancy of hexagonal geometry in [0001] direction along the c -axis. The crystallite

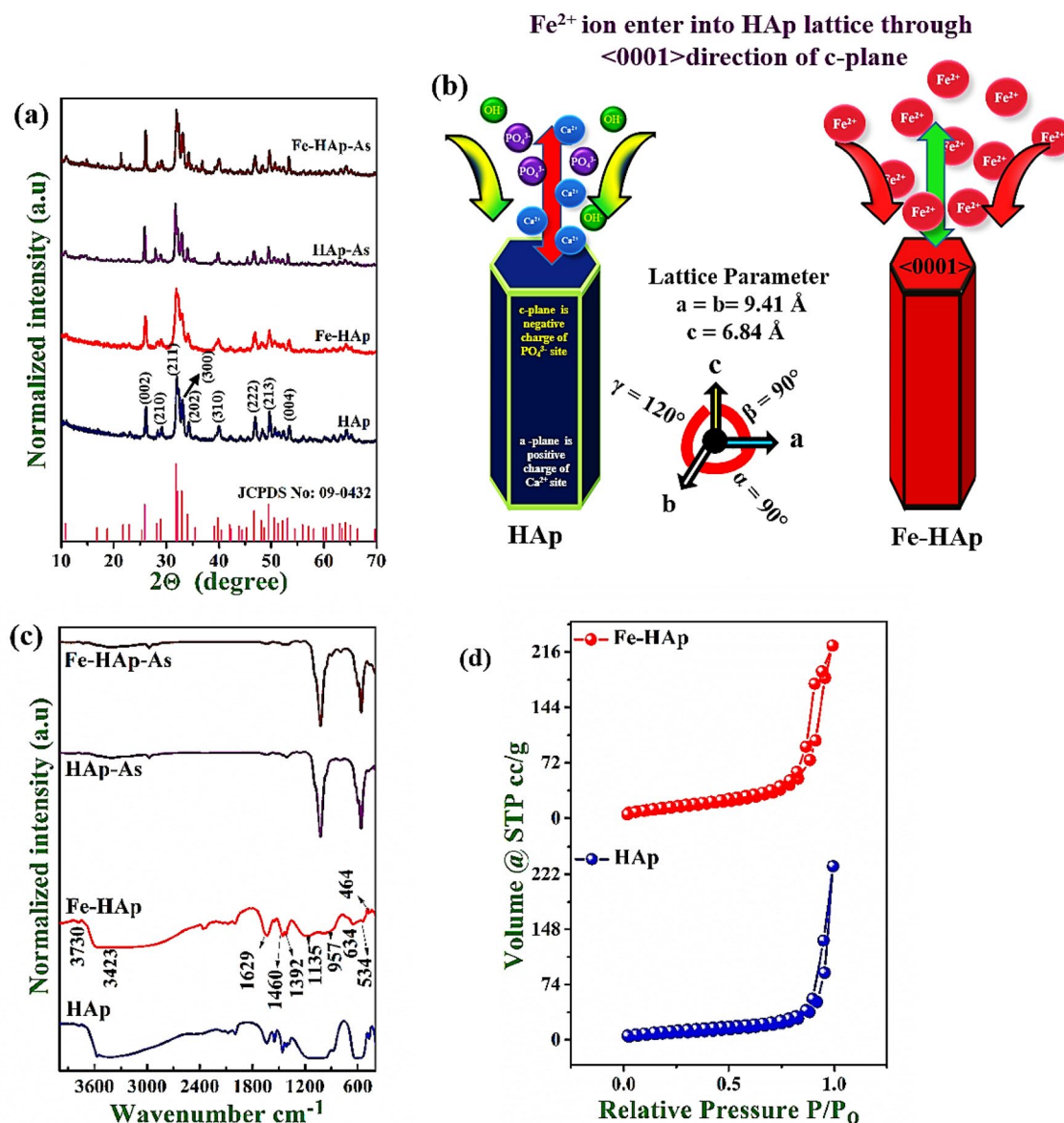


Fig. 2 a XRD pattern of HAp, Fe-HAp, HAp-As, and Fe-HAp-As, b schematic representation of growth of HAp nano-rod and Fe^{2+} ion affect the negative charge of PO_4^{3-} sites in $\langle 0001 \rangle$ direction of

c -axis, c FT-IR Spectra of HAp, Fe-HAp, HAp-As, and Fe-HAp-As, and d N_2 adsorption-desorption plot of HAp and Fe-HAp

size, crystallinity, dislocation density, and microstrain were calculated using the Eqs. (2)–(5) [3, 47–49].

$$\text{Crystallite - Size } (D_c) = \frac{K_B \lambda}{\beta \cos \theta} \quad (2)$$

$$\text{Crystallinity } (X_c) = \left(\frac{K_c}{\beta} \right)^3 \quad (3)$$

$$\text{Dislocation - density } (\delta) = \frac{1}{(D_c)^2} \quad (4)$$

$$\text{Microstrain } (\epsilon) = \left(\frac{\beta}{4 \tan \theta} \right) \quad (5)$$

where K_B is the broadening constant 0.9, λ is the wavelength of X-ray ($\lambda = 1.5414$ nm), β is full width half maximum (FWHM), K_c is constant 0.24. The incorporated Fe^{2+} ion increases microstrain (190%) and dislocation density (360%) in the crystalline plane, and peak broadening was observed to cause reduction in crystallinity and crystallite size (Fig. S1a–d) [29]. The crystallite size was calculated using the Scherrer formula from the characteristic peaks of HAp and Fe-HAp, which were 11 ± 1 nm and 6 ± 1 nm, respectively. After the adsorption of As^{3+} ions, the phase purity of HAp-As and Fe-HAp-As was analyzed by XRD. The phase purity of the adsorbent is not affected, but the full-width half maximum (FWHM) of HAp-As and Fe-HAp-As was reduced compared to HAp and Fe-HAp. Thus, the crystallite size of HAp-As and Fe-HAp-As was increased and calculated to be 27 ± 1 nm and 18 ± 1 nm, respectively (Fig. S1e). In addition, the average crystallinity of HAp and Fe-HAp was increased by adsorption of As^{3+} ion, as shown in Fig. S1f. Accordingly, a drastic reduction was observed in microstrain (61% for HAp-As and 69% for Fe-HAp-As) and dislocation density of the crystalline lattice (84% for HAp-As and 90% for Fe-HAp-As) as shown in Fig. S1g, h.

3.2 Fourier Transform Infrared Spectroscopy

The functional groups of HAp and Fe-HAp are shown in Fig. 2c. The broad absorbance band at 3458/cm and the narrow band at 3792/cm are observed due to the O–H stretching vibration. The C–O stretching vibrations are observed at 1382/cm and 1460/cm due to the absorption of CO_3^{2-} from the atmosphere [42]. The presence of OH^- in the HAp lattice was confirmed from the OH^- vibrational band observed at 1625/cm and 634/cm, which are the characteristic vibrations of HAp. The presence of bending vibration of PO_4^{3-} groups is confirmed at 464/cm and 534/cm. Symmetric and asymmetric stretching vibration of PO_4^{3-} occurred at 957/cm and 1135/cm, respectively [50]. The characteristic vibrations of

PO_4^{3-} intensity decreased at 534/cm and 634/cm due to the incorporation of Fe^{2+} ion in HAp (Fig. 2b). Since 400–600/cm is the fingerprint region of the Fe-HAp structure [44, 51, 52]. The incorporation of Fe^{2+} ions into vacant sites of HAp lattice affects the vibrational symmetry leading to the reduction in the intensity of the PO_4^{3-} group [53]. Accordingly, the FTIR spectra of HAp-As and Fe-HAp-As show the intensity reduction of hydroxyl and carbonate groups, as seen in Fig. 2c. Likewise, the stretching and bending vibrational mode of PO_4^{3-} band intensity were increased distinctly after the adsorption of As^{3+} ions due to charge neutralization with the PO_4^{3-} site. This neutralization affects the chemical environment of the phosphate ions, consequently improving the vibrational symmetry.

3.3 BET Analysis

The N_2 adsorption–desorption of HAp and Fe-HAp is shown in Fig. 2d. According to IUPAC classification, the adsorption–desorption curve of HAp and Fe-HAp indicates the type IV isotherm [54]. The pore size distribution shows the well-developed cylindrical shape mesoporous structure and the pore size is 15 ± 0.5 nm and 9 ± 0.5 nm, which corresponds to HAp and Fe-HAp. The specific surface area of HAp and Fe-HAp is 39 ± 1 m²/g and 80 ± 1 m²/g, respectively, which is listed in Table S1. The synthesized HAp has a broader pore size distribution and smaller pore volume. In contrast, the Fe-HAp exhibited a well-defined narrow pore size distribution and larger pore volume (Fig. S2) leading to an enhanced (105%) specific surface area. In addition, the synthesized Fe-HAp had a 50% smaller particle size than the HAp, further contributing to the higher specific surface area of Fe-HAp [55–57]. Consequently, the specific surface area increment lead to enhanced As^{3+} ion adsorption capacity and affinity [58].

3.4 HRSEM and HRTEM Analysis

The HRSEM images of HAp and Fe-HAp nanoparticles are shown in Fig. 3a, b, which shows uniformly distributed rod-like particles. The length of HAp was found to be 230 ± 5 nm and the width was 52 ± 5 nm; the length of Fe-HAp was 63 ± 5 nm and width was 24 ± 5 nm. Similarly, HAp-As and Fe-HAp-As exhibit a uniform distribution of rod-like morphology (Fig. 3c, d). After adsorption, the average size of the particles is increased; HAp-As is with a length of 250 ± 3 nm and width of 58 ± 3 nm; also, the length of Fe-HAp is 70 ± 3 nm and width is 30 ± 3 nm. The energy dispersive X-ray analysis (EDX) of HAp, Fe-HAp, HAp-As and Fe-HAp-As is shown in Fig. S3a–d. The EDX spectra of HAp show the presence of Ca, P, O and C elements (Fig. S3a). In addition, Fe-HAp confirms the presence of Fe^{2+} ions (Fig. S3 b). The occurrence of

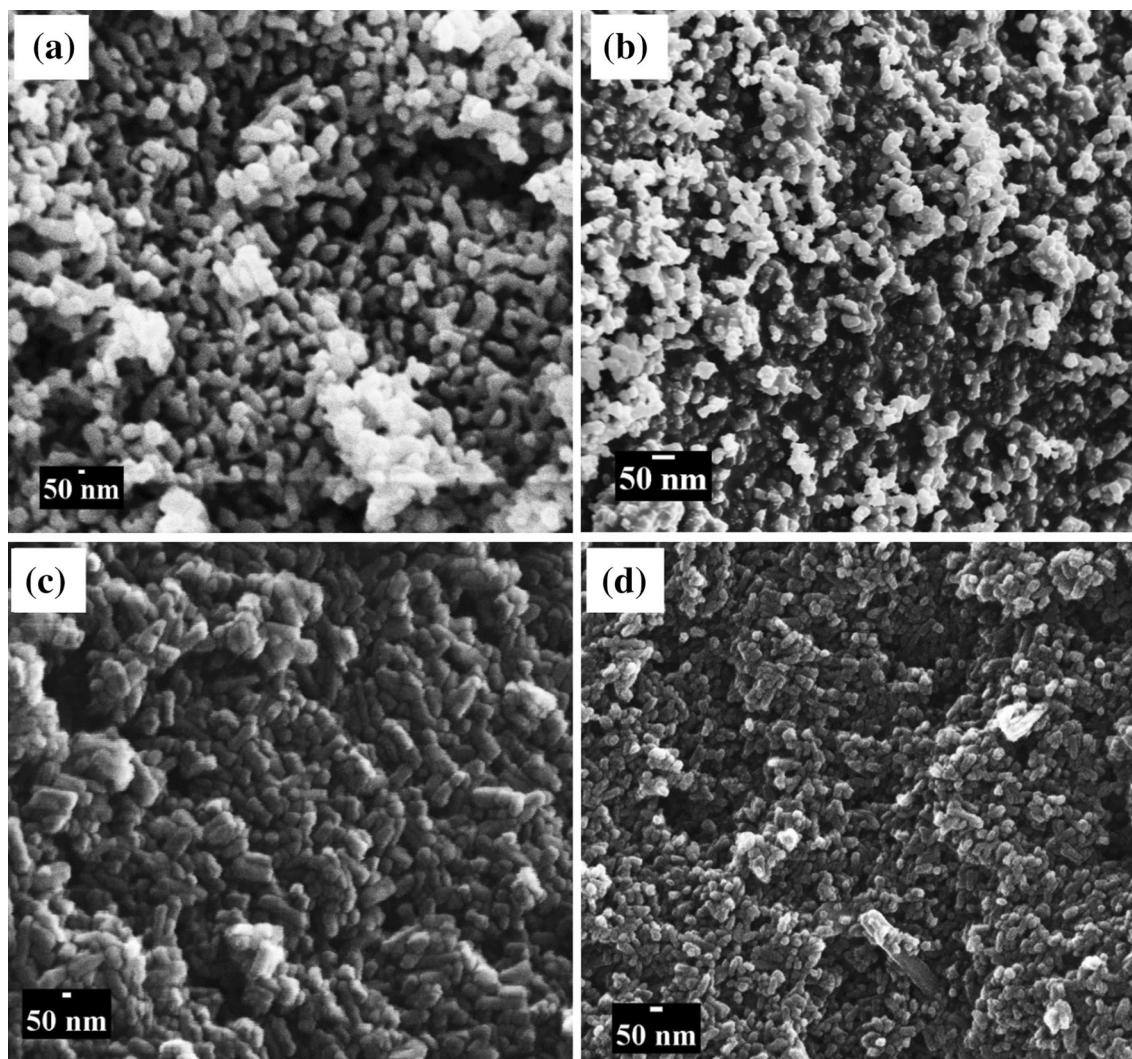


Fig. 3 HRSEM micrograph of before and after adsorption of As^{3+} ion: **a** HAp, **b** Fe-HAp, **c** HAp-As, and **d** Fe-HAp-As

Table 1 Adsorbent composition for before and after adsorption of As^{3+} ions

Adsorbents	Ca (± 1 mg/g)	P (± 1 mg/g)	Fe (0.1 mg/g)	As (3 $\mu\text{g/g}$)
HAp	437	215	–	–
HAp-As	431	212	–	134
Fe-HAp	434	210	5.1	–
Fe-HAp-As	431	209	5.04	187

the adsorbed As^{3+} was confirmed in HAp-As and Fe-HAp-As (Fig. S3 c and d). The Ca/P ratio of HAp and Fe-HAp was 1.65 and 1.64, respectively, whereas the Ca/P ratio of HAp-As is 1.52 and Fe-HAp-As is 1.53. The elemental compositions of pristine and As adsorbed samples are shown in Table 1. There was no significant variation

in the Ca/P ratio of HAp after adsorption of As^{3+} ion. These results indicate that the adsorption of As^{3+} ion is pure chemisorption rather than the ion exchange process. Hereby, HAp and Fe-HAp have been maintaining the structure and their characteristics feature after As adsorption. Furthermore, the elemental mapping of As^{3+} ion adsorbed in different pH values of HAp and Fe-HAp is shown in Fig. S4a–c. Fig. S4a shows the uniform distribution of Ca, P, C, and O for HAp and Fe-HAp. In addition, Fe-HAp shows the uniform distribution of Fe^{2+} ions as well. In pH 3, the distribution of As^{3+} ions is significantly less due to the lower colloidal stability. Whereas the distribution of As^{3+} sufficiently improved in the alkaline pH (Fig. S4b, c). However, the pH values were higher than 9.2, revealing an improper distribution of the As^{3+} ion by electrostatic repulsion between adsorbent and As^{3+} .

The HRTEM micrograph of synthesized HAp and Fe-HAp shows uniform distributions of rod-like morphology as seen in Fig. 4a, b. The dimension of HAp is 220 ± 5 nm in length and 45 ± 5 nm in width, whereas Fe-HAp is 50 ± 5 nm in length and 18 ± 5 nm in width. It was observed

that the incorporation of Fe^{2+} ions in HAp lattice significantly reduces the particle size, and narrows the pore size distribution. The enhanced specific surface area leads to an increase in the number of active sites, thereby considerably increasing the As^{3+} adsorption capacity of Fe-HAp. After

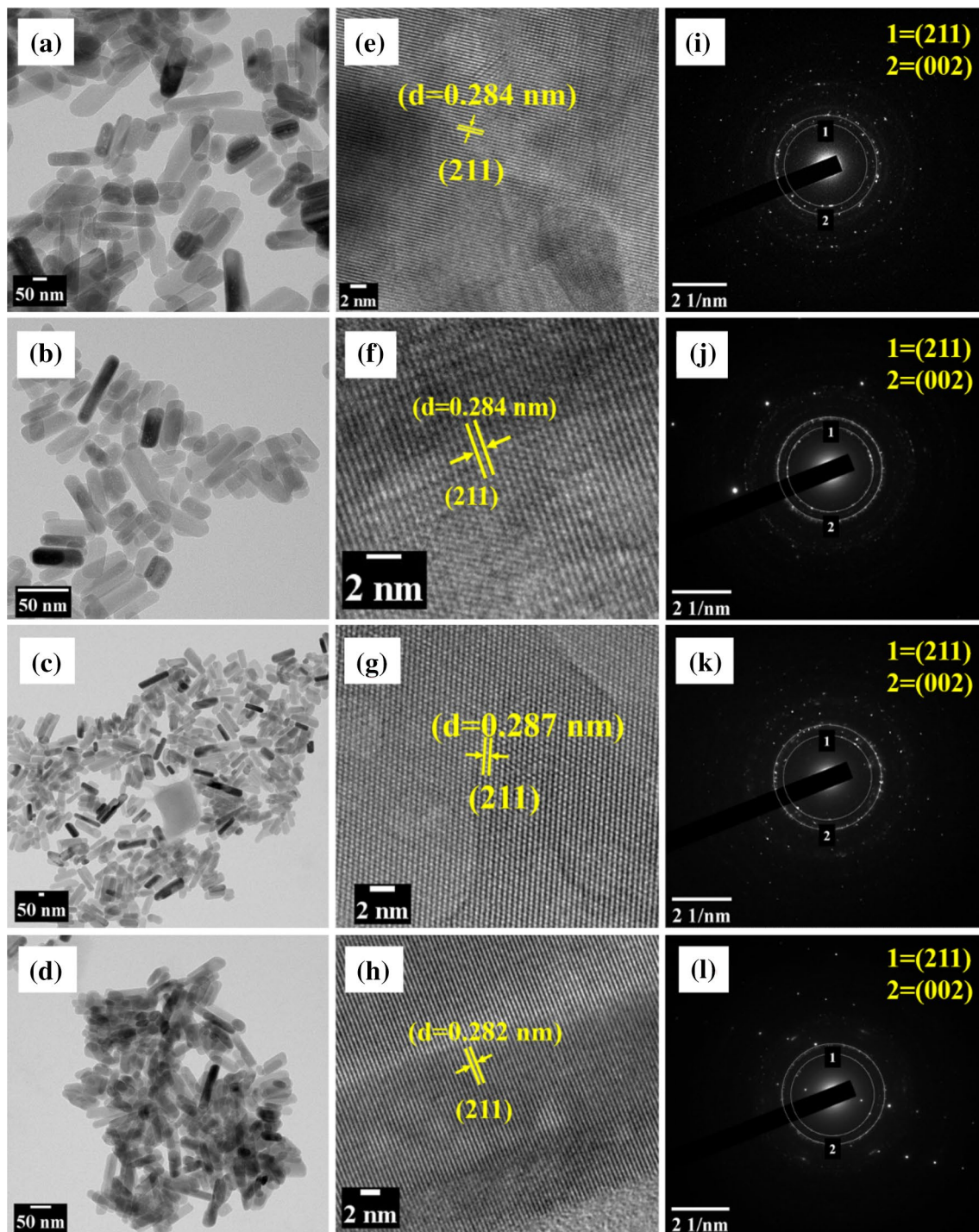


Fig. 4 HR-TEM micrographs and Selected area electron diffraction pattern of pristine and As^{3+} ion adsorbed samples **a, e, i** HAp, **b, f, j** Fe-HAp, **c, g, k** HAp-As, and **d, h, l** Fe-HAp-As

adsorption, HAp-As and Fe-HAp-As exhibit similar rod-like morphology and an increase in the particle size (Fig. 4c, d). The average size of HAp-As is 250 ± 5 nm length and 60 ± 5 nm width, whereas the average size of Fe-HAp-As is 75 ± 5 nm and width is 30 ± 5 . These results are well-matched with HRSEM particle size distribution results. The HRTEM micrograph of HAp, Fe-HAp, HAp-As, and Fe-HAp-As shows the well-resolved lattice fringes that could be observed in Fig. 4e, h, respectively. The distance between the adjacent lattices is 0.28 nm, which corresponds well with the *d*-spacing of the standard HAp phase of the (211) plane. From Fig. 4i, l, the SAED pattern reflects two sets of planes, (211) and (002), corresponding to the interplanar distance of 0.28 nm and 0.34 nm. These two diffraction planes are well-matched with the major plane of the HAp phase. Hence, the HRTEM results further confirm that the synthesized adsorbent (HAp and Fe-HAp) and As^{3+} ion adsorbed samples (HAp-As and Fe-HAp-As) are crystalline in nature and maintain the HAp phase without any major change in their rod-like morphology.

3.5 pH Effects on Zeta Potential and Isoelectric Point

The pH of the solution plays a crucial role in the adsorption process because it influences the dissociation of adsorbate ion, colloidal stability, and isoelectric point charge (pH_{pzc}) [9, 59]. Quantification of colloidal stability and pH_{pzc} in different pH values of triple distilled water and As^{3+} contaminated water are shown in Fig. 5a, b. Generally, Colloidal stability has a significant impact on the adsorption process and it was measured from zeta potential (ζ). The smaller value of the zeta potential (ζ is either positive or negative) indicates the lower colloidal stability, whereas the higher value indicates the higher colloidal stability. At lower colloidal stability, the adsorbent is more prone to change crystal structure and morphology, and increasing aggregation. Whereas, at high colloidal stability, less aggregation occurs, increasing the number of active sites on the adsorbent surface. In triple distilled water at pH 3, HAp exhibited more aggregation or lower colloidal stability due to the lower zeta potential of HAp ($\zeta = -2$ mV); whereas Fe-HAp showed the incipient stability since the zeta potential value is higher ($\zeta = -15$ mV). Hence, enhanced colloidal stability of Fe-HAp was observed in a wide range of pH at 3 to 11 due to the presence of interstitial Fe^{2+} ions in the HAp lattice. When the solution pH was increased towards alkaline, the colloidal stability of both the adsorbents significantly improved, as seen in Fig. 5a. This improvement leads to enhanced adsorption affinity and capacity by increasing surface activity. Moreover, the isoelectric point charge (pH_{pzc}) plays an essential role in adsorption by influencing the electrostatic interaction. To analyze the adsorption mechanism,

the pH_{pzc} was calculated from the pH drift method [60]. The pH_{pzc} of adsorbents HAp and Fe-HAp measured in triple-distilled water was found to be 7.1 and 7.3, respectively, as shown in Fig. 5b. Adsorbent surface charge was positive at pH value below pH_{pzc} (7 ± 0.2) due to the complexation of H^+ ions and the dissolution of phosphate ions from the adsorbent surface. The surface charge was negative when the pH value was higher than the pH_{pzc} due to complexation with OH^- ions [61].

The colloidal stability and pH_{pzc} of the adsorbents were determined from arsenic-contaminated water. The colloidal stability of HAp-As and Fe-HAp-As improved significantly with an increase in pH value 3 to 11 and also, the isoelectric point charge of the adsorbents increased from 7.1 to 8.6 for HAp-As and 7.3 to 9.3 for Fe-HAp-As. Consequently, this enhancement indicates the As^{3+} ion complexation on HAp and Fe-HAp adsorbent surface. The As^{3+} was dissociated into non-ionic state [H_3AsO_3 , $\text{As}(\text{OH})_3$] at a pH value below 9.2. Therefore the adsorption of As^{3+} on HAp and Fe-HAp was enhanced by the surface complexation process. When the pH value was above 9.2, As^{3+} dissociated into the Anionic states of $\text{As}(\text{OH})^{4-}$, $\text{AsO}_2\text{OH}^{2-}$, and the anionic states were highly repulsed by the negatively charged adsorbent as shown in the schematic representation of Fig. 5c [6, 14, 37, 61–63].

4 Adsorption

4.1 Effect of Contact Time

The determination of equilibrium contact time is essential for the adsorption process. Initially, 20 mL of 1000 $\mu\text{g/L}$ As^{3+} solution in pH 7 was mixed with 100 mg of HAp and Fe-HAp in different sterilized containers. The mixture of the solution was stirred (180 rpm) at room temperature (25 ± 1 °C) for different time intervals. The adsorption capacity of As^{3+} in the various time intervals was calculated and it is shown in Fig. 5d. The whole adsorption process can be divided into two stages as linear and equilibrium of As^{3+} adsorption. The adsorption capacity was found to increase with contact time and the maximum capacity was achieved at 10 min. After that, the adsorption turned sluggish and reached equilibrium. Hence, an equilibrium adsorption time of 10 min was fixed for the subsequent study of As^{3+} adsorption. Kinetic isotherm was used to understand the adsorption rate and adsorption mechanism of As^{3+} on the surface of HAp and Fe-HAp.

4.2 Effect of the Initial Concentration of As^{3+}

The maximum adsorption capacity of HAp and Fe-HAp obtained by varying the initial concentration of As^{3+} ion

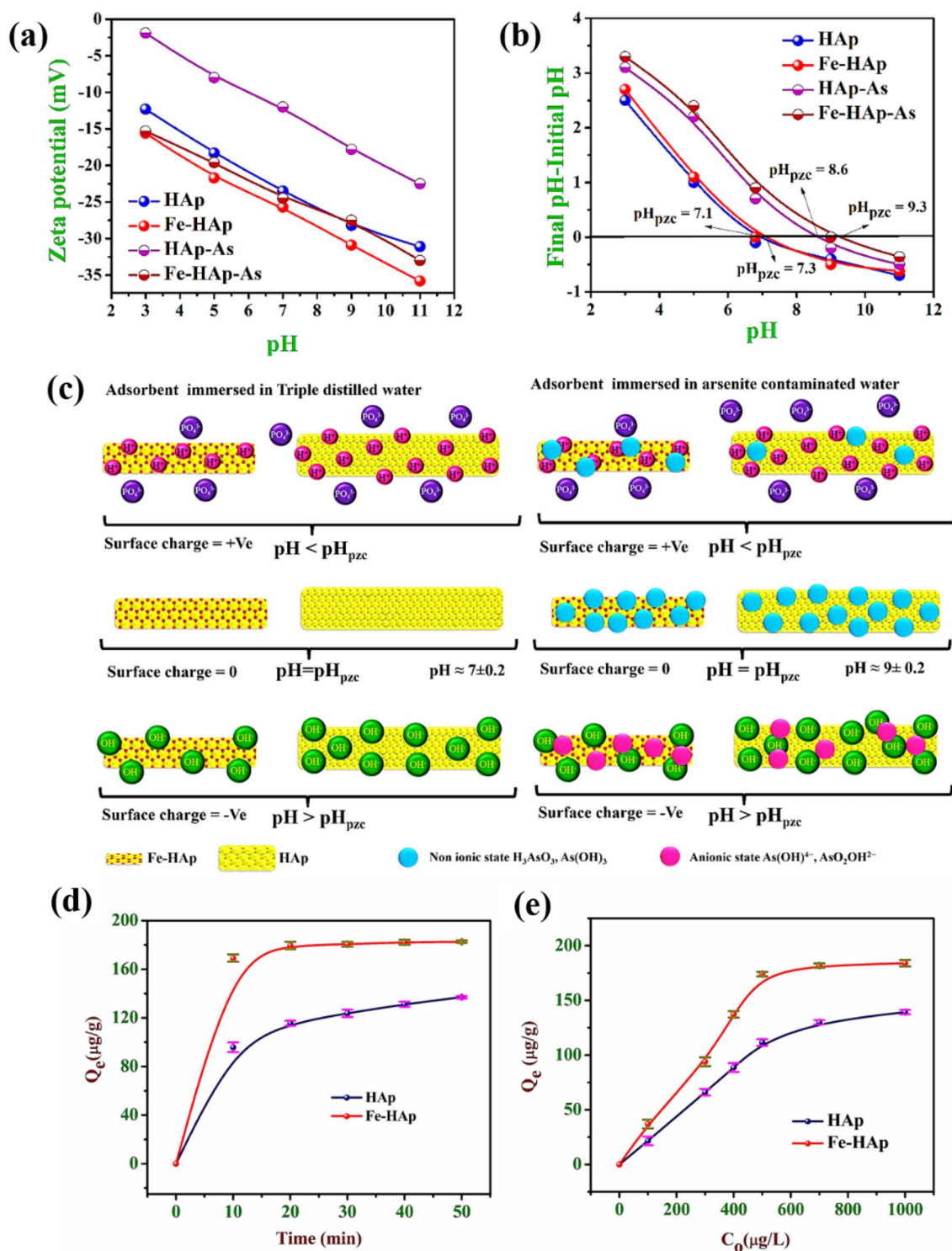


Fig. 5 Effect of pH on HAp, Fe-HAp, HAp-As, and Fe-HAp-As in deionized water and As³⁺ ion contaminated water: **a** zeta potential, **b** point zero charge, **c** schematic representation of pH affect the zero pint charge for before and after adsorption of As³⁺ ion, **d** effect of

contact time [pH=7; concentration=1000 μg/L; dosage=100 mg; rpm=180 and temperature=298 K], and **e** effect of initial concentration of As³⁺ [pH=7; Time=10 min; dosage=100 mg; rpm=180 and temperature=298 K]

(100–1000 $\mu\text{g/L}$) is shown in Fig. 5e. 100 mg of HAp and Fe-HAp were taken into different sterilized containers with various initial concentrations of As^{3+} solution (pH 7) at room temperature (25 ± 1 °C). The contact time was fixed at the equilibrium time (10 min), and the shaking speed was set to be 180 rpm. The removal capacity of both adsorbents improved with the increasing initial concentration of As^{3+} . This indicates that the higher initial concentration of As^{3+} enhanced adsorbate mobility, driving force and reduced mass transfer resistance between adsorbate and adsorbent [64]. The adsorption of As^{3+} was increased up to a concentration of 500 $\mu\text{g/L}$ thereafter, adsorption attained equilibrium. The equilibrium adsorption capacity of As^{3+} on HAp and Fe-HAp was found to be 139 ± 2 $\mu\text{g/g}$ and 183 ± 2 $\mu\text{g/g}$, respectively.

4.3 Effect of Competing Ions and Regeneration Efficiency of As^{3+} Adsorption

The natural water source contains various types of ions with different characteristics such as phosphate (PO_4^{3-}), sulfate (SO_4^{2-}), carbonate (CO_3^{2-}), nitrate (NO_3^-), and chloride (Cl^-), which compete with each other to adhere on to the adsorbent active sites. The adsorption of As^{3+} ions on HAp and Fe-HAp in the presence of other competing ions is shown in Fig. 6a. The concentration of As^{3+} ions and other competing ions was fixed at 1000 $\mu\text{g/L}$. The influence of other competing ions on the adsorption of the As^{3+} ion process was carried out at room temperature (298 K) fixing the pH of the adsorbate solution at 7 and the equilibrium time at 10 min. The respective adsorption capacities of HAp and Fe-HAp were 139 ± 2 $\mu\text{g/g}$ and 183 ± 2 $\mu\text{g/g}$ in the absence of other competing ions. In the presence

of other competing ions, the adsorption capacity of HAp decreased by 19% (139 $\mu\text{g/g}$ to 113 $\mu\text{g/g}$). The competing ions reduced the As^{3+} adsorption capacity of HAp in the order of $\text{CO}_3^{2-} > \text{SO}_4^{2-} > \text{PO}_4^{3-} > \text{NO}_3^- > \text{Cl}^-$; suggesting that the affinity or selectivity of As^{3+} ion on HAp is low in the presence of other competing ions. The Fe-HAp did not show any significant decrease in the adsorption capacity in the presence of competing ions suggesting that the affinity or selectivity of As^{3+} ion on Fe-HAp is higher than other competing ions.

Reusability is essential for practical application and greatly enhances the adsorbent durability. The As^{3+} ion adsorbed samples were regenerated using diluted 0.1 M of HCl to treat the HAp-As and Fe-HAp-As. The synthesized adsorbents were subjected to seven consecutive regeneration cycles, as shown in Fig. 6b. The results revealed that the As^{3+} removal capacity of HAp gradually decreased to 74% (139 to 36 $\mu\text{g/g}$) whereas the Fe-HAp exhibited sustained regeneration efficiency (97%) up to 7 cycles. These results indicate that the Fe-HAp maintains colloidal stability compared to HAp during the regeneration process. Moreover, these results agree with the zeta potential results of HAp and Fe-HAp (Fig. 5a).

4.4 Adsorption Isotherm

4.4.1 Kinetic Isotherm

The experimental kinetic data were fitted to two different isotherms, such as Lagergren pseudo-first and Lagergren pseudo-second-order kinetics [65]. The first and second-order kinetics reveal the physisorption and chemisorption,

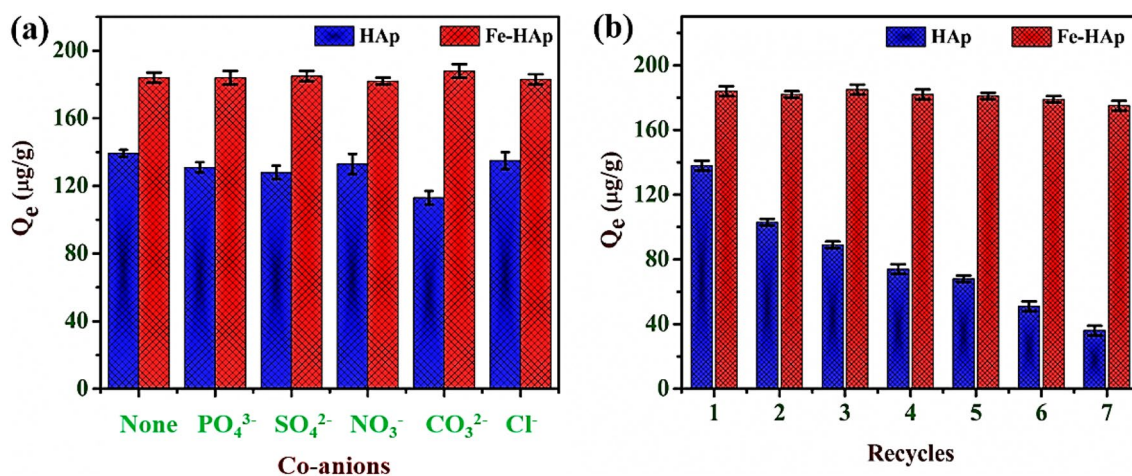


Fig. 6 **a** Competing ions effect of As^{3+} ion adsorption on HAp and Fe-HAp [pH=7; time=10 min; concentration=1000 $\mu\text{g/L}$; dosage=100 mg; rpm=180 and temperature=298 K], and **b** regen-

eration of As^{3+} ion by HAp and Fe-HAp [pH=7; time=10 min; concentration=1000 $\mu\text{g/L}$; dosage=100 mg; rpm=180 and temperature=298 K]

respectively. The linear fit expression of first and second-order kinetics is given in Eqs. (6), (7).

$$\text{Log}(Q_e - Q_t) = \text{Log}(Q_e) - \left(\frac{K_1}{2.303}\right)t \quad (6)$$

$$\frac{t}{Q_t} = \frac{1}{(K_2 \times Q_e^2)} + \left(\frac{1}{Q_t}\right)t \quad (7)$$

where Q_t and Q_e represent the given time and equilibrium adsorption capacity ($\mu\text{g/g}$), respectively, K_1 is the first-order rate constant (min^{-1}). The values of Q_e and K_1 were determined from intercept and slope in the linear fit of $\log(Q_e - Q_t)$ as a function of time t , as shown in Fig. 7a. K_2 is the second-order rate constant ($\text{g}/\mu\text{g min}^{-1}$). The values of K_2 and Q_e

were calculated from the intercept and slope in a linear plot of $1/Q_t$ as a function of time t , as shown in Fig. 7b [66, 67].

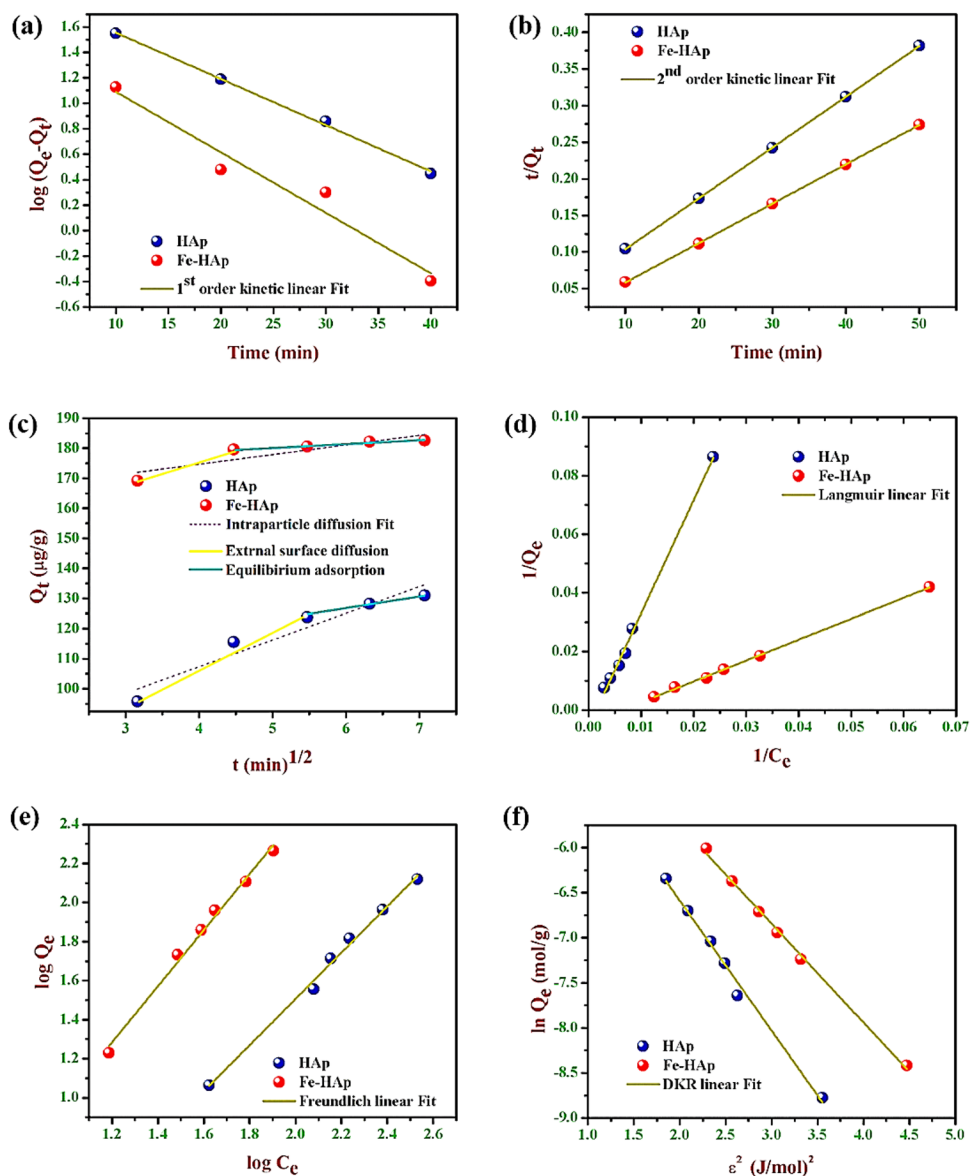
4.4.2 Intra-Particle Diffusion

The intra-particle diffusion isotherm was used to find the rate-controlling mechanism of As^{3+} diffusion on HAp and Fe-HAp during the adsorption [5]. The linear expression of the intra-particle diffusion is given in Eq. (8).

$$Q_t = K_i \sqrt{t} + C_i \quad (8)$$

where K_i is the intra-particle diffusion rate constant ($\mu\text{g/g min}^{-1/2}$) and C_i is the boundary layer thickness of As^{3+} adsorption. Further, K_i and C_i can be calculated from the

Fig. 7 As^{3+} ion adsorption isotherms of HAp and Fe-HAp: **a** pseudo 1st order kinetics, **b** pseudo 2nd order kinetics, **c** intra particle diffusion, **d** langmuir, **e** freundlich, and **f** DKR



slope and intercept of intra-particle diffusion linear fit of Q_t as a function of \sqrt{t} as shown in Fig. 7c [68].

The linear regression of R^2 is well matched in second-order kinetics compared to first-order kinetics. Also, the adsorption capacities of theoretical and experimental values are in good agreement with second-order kinetics. Hence, it confirms the chemisorption of As^{3+} on HAp and Fe-HAp. The second-order rate constant (K_2) indicates that the adsorption rate (1 min) and their capacity ($Q_e = 538\%$) are higher for Fe-HAp when compared to HAp nanoparticles (Table 2). The As^{3+} adsorption on HAp and Fe-HAp shows the two-stage adsorption process. Initially, the linear portion revealed the adsorption of As^{3+} as a combination of surface and pore diffusion processes. The last linear part represents the equilibrium adsorption, as shown in Fig. 7c.

4.4.3 Langmuir, Freundlich, and DKR Isotherm

The equilibrium adsorption of As^{3+} is either a monolayer or multilayer distribution, which is determined from Langmuir and Freundlich isotherm, respectively. In monolayer adsorption, active sites on the adsorbent surface are distinct and identical [69, 70]. The linear expression of Langmuir isotherm is given by Eq. (9).

$$\frac{C_e}{Q_e} = \frac{1}{Q_m K_L} + \frac{C_e}{Q_m} \quad (9)$$

where C_e represents the equilibrium concentration ($\mu\text{g/L}$), K_L is Langmuir isotherm constant ($\text{L}/\mu\text{g}$), suggesting the adsorption affinity (or) sensitivity, and Q_m is theoretical monolayer adsorption capacity ($\mu\text{g/g}$). The values of Q_m and K_L are calculated from the intercept and slope in a linear fit of $1/C_e$ vs. $1/Q_e$, as shown in Fig. 7d. The essential feature of Langmuir is a dimensionless constant called the separation factor (R_L), which is given as Eq. (10). The value of the R_L indicates the various types of adsorption, such as linear ($R_L = 1$), unfavorable ($R_L > 1$), favorable ($0 < R_L < 1$) and irreversible ($R_L = 0$) [71]. Freundlich isotherm explains multilayer adsorption on heterogeneous surfaces and it gives the empirical relationship between the adsorbate and adsorbent, the linear expression of Freundlich isotherm is given by Eq. (11) [59, 72].

$$R_L = \frac{1}{(1 + K_L C_o)} \quad (10)$$

$$\text{Log} Q_e = \log K_F + \left(\frac{1}{n}\right) \log C_e \quad (11)$$

where K_F is the adsorption capacity ($\mu\text{g/g}$) of Freundlich isotherm and $1/n$ is the Freundlich exponent. The values of K_F and $1/n$ are determined from the intercept and slope of the linear fit of $\log C_e$ vs. $\log Q_e$ as shown in Fig. 7e. The value of $1/n$ indicates the adsorption behavior as it is linear [$(1/n) = 1$] or unfavorable [$(1/n) > 1$] or favorable [$0.1 < (1/n) < 1$] or irreversible [$(1/n) = 0$].

The Dubinin–Radushkevich isotherm is generally applied to distinguish between physisorption and chemisorption based on the Gaussian energy distribution. The physisorption process occurs when the atom/molecule is adsorbed by Van der Waals force of the material, whereas chemisorption occurs either by valence electron sharing or ion exchange between adsorbate and adsorbent [73–75]. The linear expression of Dubinin–Radushkevich isotherm is given in Eq. (12).

$$\ln Q_e = \ln Q_m - \beta \varepsilon^2 \quad (12)$$

$$\varepsilon = RT \ln \left(1 + \frac{1}{C_e}\right) \quad (13)$$

where β is DKR constant; it gives adsorption mean energy (mol/J)². ε is Polanyi potential expressed in Eq. (13); Q_m is maximum adsorption capacity ($\mu\text{g/g}$), R is the universal gas constant 8.314 (J/mol K) , and T is the absolute temperature (K). β and Q_m can be calculated from the slope and intercept of the $\ln Q_e$ vs. ε^2 linear fit, as shown in Fig. 7f. The adsorption is divided into three types based on the value of

Table 2 Adsorption isotherm of As^{3+} ion adsorption using HAp and Fe-HAp

	Adsorbent	Adsorbent	
		HAp	Fe-HAp
	* Q_{exp} ($\mu\text{g/g}$)	132 ± 5	184 ± 5
Pseudo-first-order kinetics	Q_m ($\mu\text{g/g}$)	83 ± 3	37 ± 3
	K_1 (/min)	0.036	0.047
	R^2	0.9971	0.9360
Pseudo-second-order	Q_m ($\mu\text{g/g}$)	144 ± 3	188 ± 3
	K_2 ($\mu\text{g/g min}^{-1}$)	28.9 ± 1	185 ± 1
	R^2	0.9999	0.9999
Intra-particle diffusion	K_i ($\mu\text{g/g min}^{1/2}$)	8.85 ± 0.1	3.20 ± 0.1
	C_i ($\mu\text{g/g}$)	71.94 ± 1	161.84 ± 1
	R^2	0.9035	0.8314
Langmuir isotherm	Q_m ($\mu\text{g/g}$)	139 ± 3	183 ± 3
	K_L ($\mu\text{g/L}$)	3.85	0.71
	R_L	$3.8e^{-3}$	$7.11e^{-4}$
	R^2	0.9966	0.9989
Freundlich isotherm	K_F ($\mu\text{g/g}$)	7.31 ± 2	2.77 ± 2
	$1/n$	1.18	1.43
	R^2	0.9932	0.9900
DKR	Q_m ($\mu\text{g/g}$)	127 ± 2	181 ± 2
	β (mol/J^2)	$-1.439e^{-9}$	$-1.096e^{-9}$
	E (kJ/mol)	18.6 ± 0.1	21.3 ± 0.1
	R^2	0.9907	0.9970

* Q_{exp} is experimental adsorption capacity ($\mu\text{g/g}$)

Gaussian energy (E) distribution as given in Eq. (14). They are physisorption ($E < 8$ kJ/mol), chemical ion exchange (8 kJ/mole $\leq E \leq 16$ kJ/mole), and strong chemisorption than ion exchange ($E > 16$ kJ/mol) [76]. The adsorption of As^{3+} will follow any one of the above-mentioned adsorption processes.

$$E = \frac{1}{\sqrt{-2\beta}} \quad (14)$$

The linear fit of Langmuir, Freundlich and DKR isotherms is shown in Fig. 7d–f. The linear regression R^2 values are well-matched with the Langmuir isotherm compared to the Freundlich and DKR isotherms. Also, the experimental and theoretical values of the As^{3+} adsorption capacity are better suited for Langmuir and DKR isotherm than the Freundlich isotherm. Moreover, separation factor RL indicates that the adsorption favored Langmuir isotherm. Hence the adsorption of As^{3+} monolayer was confirmed. The maximum adsorption capacity of As^{3+} on HAp and Fe-HAp is 139 ± 2 $\mu\text{g/g}$ and 183 ± 2 $\mu\text{g/g}$, respectively. The As^{3+} adsorption affinity or sensitivity was found to be 3.85 $\mu\text{g/L}$ for HAp and 0.71 $\mu\text{g/L}$ for Fe-HAp (shown in Table 2). The adsorption affinity of Fe-HAp was enhanced at the trace level (≤ 50 $\mu\text{g/L}$), which is 83–99% higher than the previous reports, as shown in Table 3. The Gaussian energy distribution on HAp and Fe-HAp is 18.6 kJ/mol and 21.3 kJ/mol, respectively and these results suggest stronger chemical adsorption than the ion-exchange process.

The hydrothermally synthesized HAp and Fe-HAp reported in this work possess the nanostructured uniform size and shape along with high surface area. In comparison with HAp, the Fe doped HAp shows high surface area, which results in enhancing the adsorption rate, capacity, regeneration efficiency, stability and affinity. Moreover, the Fe-HAp is a non-toxic and low-cost adsorbent. The comparison with the adsorbents already existing in the literature is

provided in Table 3. The reported adsorbents, such as iron-oxide-coated quartz (IOCQ) [19], magnetic Fe-hydroxalcite [21], activated alumina [22], sulfate-modified iron oxide-coated sand [23], Iron oxide-coated sand [26], 6%Cu-HAp3 [24], and HAp from fish scale [25] exhibit very low arsenic adsorption capacity, affinity and adsorption rate. Even though the biochar [20] and $\text{Fe}_2\text{O}_3\text{-ZrO}_2/\text{BC}$ [27] show higher capacity than the Fe-HAp, the adsorption rate of biochar and $\text{Fe}_2\text{O}_3\text{-ZrO}_2/\text{BC}$ is fairly low compared to Fe-HAp. Moreover, Fe-HAp shows a rapid equilibrium process (1 min) due to its higher adsorption affinity (83–99%) at trace level (≤ 50 $\mu\text{g/L}$). In addition, the regeneration efficiency of $\text{Fe}_2\text{O}_3\text{-ZrO}_2/\text{BC}$ is gradually decreased from 97 to 29% (from 1 to 6th cycle) whereas, Fe-HAp exhibits sustained regeneration efficiency (97%) up to 7th cycle of regeneration. Furthermore, in the presence of other competing ions, there was no significant decrease in As^{3+} ion absorption. Hence, the synthesized Fe-HAp is comparatively stable and could be considered a potential adsorbent for the removal of arsenic ions from water compared to the other reported adsorbents.

5 Quantification of Fe^{2+} Ion Release Test

Fig. S5 shows the quantification of Fe^{2+} ion in HAp nanoparticle (Sample C) and also Fe^{2+} leached from As^{3+} contaminated water (Sample B), and triple distilled water (Sample A). The concentration of Fe^{2+} ion on Fe-HAp was estimated to be 5.06 ± 0.05 mg/g. The concentration of Fe^{2+} ion released in triple-distilled water and As^{3+} contaminated water was found to be 0.005 ± 0.001 mg/L and 0.019 ± 0.001 $\mu\text{g/L}$, respectively, which is 600 times below the acceptable level of iron in drinking water (1–3 mg/L) [77]. A very low quantity of iron incorporation leads to highly efficient adsorption of As^{3+} and confirms the insignificant release of iron during the adsorption process.

Table 3 Comparison of arsenic adsorption capacity of various adsorbents reported in the literature

Adsorbent	Time (min)	pH	Adsorption Capacity (mg/g)	Arsenic oxidation state	Affinity (mg/L)	Ref
Iron-oxide-coated quartz (IOCQ)	5	6	0.097	As^{5+}	–	[19]
Biochar	1440	7	0.422	As^{5+}	41.49	[20]
Magnetic Fe-hydroxalcite	15	9	0.121	As^{3+}	0.014	[21]
Activated alumina	360	7.6	0.180	As^{3+}	0.117	[22]
Sulfate-modified iron oxide-coated sand	480	7.2	0.096	As^{3+}	0.326	[23]
Iron oxide-coated sand	180	7.5	0.028	As^{3+}	0.012	[26]
6%Cu-HAp3	60	9	0.070	As^{5+}	–	[24]
HAp from fish scale	3000	4	0.024	As^{3+}	0.192	[25]
$\text{Fe}_2\text{O}_3\text{-ZrO}_2/\text{BC}$	120	7	0.538	As^{3+}	0.032	[27]
Fe-HAp (Iron-Hydroxyapatite)	1	7	0.183	As^{3+}	7.11e^{-4}	This work

6 Conclusion

The HAp and Fe-HAp nanorods were synthesized via a simple and cost-effective hydrothermal method to remove As^{3+} ions. Merely 0.5 wt% of Fe^{2+} ion is incorporated in the HAp, which results in enhanced physiochemical properties of the adsorbent and improves adsorption of As^{3+} . The doping of Fe^{2+} ion in HAp improves the colloidal stability, particle size (Drastic reduction of 400% in length and 225% in width), and specific surface area (105% higher than the HAp). As a result, more active sites are formed in Fe-HAp than HAp, which leads to obtaining a maximum adsorption capacity of As^{3+} . The maximum adsorption capacity of As^{3+} is $183 \pm 2 \mu\text{g/g}$ with a higher adsorption rate (538%) at trace level contamination ($\leq 50 \mu\text{g/L}$). In addition, the dopant Fe^{2+} ion ensures a higher adsorption affinity (83–99%) compared to values previously reported literature. The incorporated Fe^{2+} ion sustained 97% regeneration efficiency up to 7th cycle and maintained the maximum adsorption in the presence of other competing ions. The adsorption of As^{3+} ion does not change the hydroxyapatite phase and morphology. From isotherm theoretical evaluation, the adsorption of the As^{3+} ion was confirmed to be monolayer chemisorption rather than the ion-exchange process. Furthermore, quantification of iron studies showed a very lower concentration (0.005 to 0.019 mg/L) of Fe^{2+} ion, which leaked during the adsorption process and it was 600 times lower than the WHO toxic limits of iron in the water. Hence, the Fe-HAp is a cost-effective, potential adsorbent, and promising for removing highly toxic As^{3+} even at trace level ($\leq 50 \mu\text{g/L}$) and maintaining water quality.

Supplementary Information The online version contains supplementary material available at <https://doi.org/10.1007/s10904-021-02103-0>.

Acknowledgements The authors would like to thank the government of India for the financial support from the Department of Science And Technology through the scheme of Technology Development Programme -1010 [No: DST/TM/WTI/2K16/219(G)-A]. One of the authors (Subbaraya Narayana Kalkura) thanks the University Grants Commission, India, for the award of the Basic Scientific Research (UGC-BSR) Faculty Fellowship [No. F.4-5(11)2019 (BSR)].

Author Contributions SEP: conceptualization, methodology, writing—original draft. SS: validation, investigation. VR: writing—review and editing. EK: writing—review and editing. SJP: formal analysis, writing—review and editing. HCS: writing—review and editing. SNK: writing—review and editing, supervision, investigation, project administration.

Declarations

Conflict of interest The authors declare that they have no known competing financial interests or personal relationships that could have influenced the work reported in this paper. This article is original and new, has been written by the stated authors who are all aware of its

content and approve its submission. The article has not been published previously, it is not under consideration for publication elsewhere, and no conflict of interest exists. The article will not be published elsewhere in the same form, in any language, without the written consent of the publisher.

References

1. D.E. Baker, L. Chesnin, *Adv. Agron.* **27**, 305 (1975)
2. D. Mohan, C.U. Pittman, J. Hazard. Mater. **142**, 1 (2007)
3. W. Jiang, X. Chen, Y. Niu, B. Pan, J. Hazard. Mater. **243**, 319 (2012)
4. T.K. Das, T.S. Sakthivel, A. Jeyaranjan, S. Seal, A.N. Bezbaruah, *Chemosphere* **253**, 126702 (2020)
5. X. Min, C. Zhou, C. Han, J. Tang, D. Liu, Y. Luo, J. Mater. Sci. **55**, 8145 (2020)
6. V.M. Boddu, K. Abburi, J.L. Talbott, E.D. Smith, R. Haasch, *Water Res.* **42**, 633 (2008)
7. I. Andjelkovic, D. Stankovic, J. Nesic, J. Krstic, P. Vulic, D. Manojlovic, G. Roglic, *Ind. Eng. Chem. Res.* **53**, 10841 (2014)
8. S. Yao, Z. Liu, Z. Shi, *J. Environ. Health Sci. Eng.* **12**, 6 (2014)
9. L.L. Min, L. Bin Zhong, Y.M. Zheng, Q. Liu, Z.H. Yuan, L.M. Yang, *Sci. Rep.* **6**, 32480 (2016)
10. C.K. Jain, I. Ali, *Water Res.* **34**, 4304 (2000)
11. M. Khatamian, N. Khodakarampoor, M. Saket-Oskoui, *J. Colloid Interface Sci.* **498**, 433 (2017)
12. P. Mondal, C.B. Majumder, B. Mohanty, *J. Hazard. Mater.* **137**, 464 (2006)
13. L.H. Velazquez-Jimenez, J.A. Arcibar-Orozco, J.R. Rangel-Mendez, *J. Environ. Manag.* **212**, 121 (2018)
14. N. Zhu, J. Qiao, Y. Ye, T. Yan, *J. Environ. Manag.* **211**, 73 (2018)
15. P. Sabbatini, F. Yrazu, F. Rossi, G. Thern, A. Marajofsky, M.M. Fidalgo de Cortalezzi, *Water Res.* **44**, 5702 (2010)
16. H. Chen, J. Li, X. Wu, X. Wang, *Ind. Eng. Chem. Res.* **53**, 16051 (2014)
17. C.S. Fan, S.C. Tseng, K.C. Li, C.H. Hou, *J. Hazard. Mater.* **312**, 208 (2016)
18. J. Kamieniak, P.J. Kelly, C.E. Banks, A.M. Doyle, *J. Inorg. Organomet. Polym. Mater.* **28**, 84 (2018)
19. M.G. Mostafa, Y.H. Chen, J.S. Jean, C.C. Liu, H. Teng, *Water Sci. Technol.* **62**, 378 (2010)
20. X. Gao, Y. Peng, L. Guo, Q. Wang, C.Y. Guan, F. Yang, Q. Chen, *J. Environ. Manag.* **271**, 111045 (2020)
21. T. Türk, I. Alp, *J. Ind. Eng. Chem.* **20**, 732 (2014)
22. T.S. Singh, K.K. Pant, *Sep. Purif. Technol.* **36**, 139 (2004)
23. R.C. Vaishya, S.K. Gupta, *J. Chem. Technol. Biotechnol.* **78**, 73 (2003)
24. S.A. Jahan, M.Y.A. Mollah, S. Ahmed, M.A.B.H. Susan, *J. Sci. Res.* **9**, 383 (2017)
25. M.S. Rahaman, A. Basu, M.R. Islam, *Bioresour. Technol.* **99**, 2815 (2008)
26. V.K. Gupta, V.K. Saini, N. Jain, *J. Colloid Interface Sci.* **288**, 55 (2005)
27. S.I. Siddiqui, S.A. Chaudhry, *J. Clean. Prod.* **223**, 849 (2019)
28. Y. Li, S. Wang, Y. Zhang, R. Han, W. Wei, *J. Mol. Liq.* **247**, 171 (2017)
29. D.F. Mercado, G. Magnacca, M. Malandrino, A. Rubert, E. Montoneri, L. Celi, A. Bianco Prevot, M.C. Gonzalez, *ACS Appl. Mater. Interfaces* **6**, 3937 (2014)
30. S. Saber-Samandari, S. Saber-Samandari, N. Nezafati, K. Yahya, *J. Environ. Manag.* **146**, 481 (2014)
31. X. Xiao, L. Yang, D. Zhou, J. Zhou, Y. Tian, C. Song, C. Liu, *Colloids Surf. A Physicochem. Eng. Asp.* **555**, 548 (2018)
32. H.L. Lien, R.T. Wilkin, *Chemosphere* **59**, 377 (2005)

33. X.H. Guan, J. Wang, C.C. Chusuei, J. Hazard. Mater. **156**, 178 (2008)
34. A. Masoumi, M. Ghaemy, A.N. Bakht, Ind. Eng. Chem. Res. **53**, 8188 (2014)
35. D. Dickson, G. Liu, Y. Cai, J. Environ. Manag. **186**, 261 (2017)
36. I. Mayer, H. Diab, I. Felner, J. Inorg. Biochem. **45**, 129 (1992)
37. A.F. de Namor, N. Al Hakawati, W.A. Hamdan, R. Soualhi, S. Korfali, L. Valiente, J. Hazard. Mater. **326**, 61 (2017)
38. N. Kataria, V.K. Garg, Chemosphere **208**, 818 (2018)
39. B. Hu, L. Wu, M. Ou, X. Wang, Y. Tang, J. Inorg. Organomet. Polym. Mater. **31**, 2627 (2021)
40. M. Ashok, N. Meenakshi Sundaram, S. Narayana Kalkura, Mater. Lett. **57**, 2066 (2003)
41. E. Kolanthai, K. Ganesan, M. Epple, S.N. Kalkura, Mater. Today Commun. **8**, 31 (2016)
42. V. Sarath Chandra, G. Baskar, R.V. Suganthi, K. Elayaraja, M.I. Ahymah Joshy, W. Sofi Beaula, R. Mythili, G. Venkatraman, S. Narayana Kalkura, ACS Appl. Mater. Interfaces **4**, 1200 (2012)
43. P. Kanchana, N. Lavanya, C. Sekar, Mater. Sci. Eng. C **35**, 85 (2014)
44. J. Trinkunaite-Felsen, A. Prichodko, M. Semasko, R. Skaudzius, A. Beganskiene, A. Kareiva, Adv. Powder Technol. **26**, 1287 (2015)
45. K. Lin, J. Chang, X. Liu, L. Chen, Y. Zhou, CrystEngComm **13**, 4850 (2011)
46. M. Okada, T. Matsumoto, Jpn. Dent. Sci. Rev. **51**, 85 (2015)
47. Z.Y. Li, W.M. Lam, C. Yang, B. Xu, G.X. Ni, S.A. Abbah, K.M.C. Cheung, K.D.K. Luk, W.W. Lu, Biomaterials **28**, 1452 (2007)
48. V. Mote, Y. Purushotham, B. Dole, J. Theor. Appl. Phys. **6**, 2 (2012)
49. H. Kamal, A.M. Hezma, Phys. Sci. Int. J. **7**, 137 (2015)
50. A. Destainville, E. Champion, D. Bernache-Assollant, E. Laborde, Mater. Chem. Phys. **80**, 269 (2003)
51. Y.S. Li, J.S. Church, A.L. Woodhead, J. Magn. Magn. Mater. **324**, 1543 (2012)
52. O. Kaygili, S.V. Dorozhkin, T. Ates, A.A. Al-Ghamdi, F. Yakuphanoglu, Ceram. Int. **40**, 9395 (2014)
53. H. Shi, F. He, J. Ye, J. Mater. Chem. B **4**, 1712 (2016)
54. Z.A. Allothman, Materials (Basel) **5**, 2874 (2012)
55. R.C. Pawar, V. Khare, C.S. Lee, Dalton Trans. **43**, 12514 (2014)
56. S.A. Idris, K.M. Alotaibi, T.A. Peshkur, P. Anderson, M. Morris, L.T. Gibson, Microporous Mesoporous Mater. **165**, 99 (2013)
57. N. Jayaprakash, S.S. Moganty, X.W. Lou, L.A. Archer, Appl. Nanosci. **1**, 7 (2011)
58. C. Zhang, W. Wang, A. Duan, G. Zeng, D. Huang, C. Lai, X. Tan, M. Cheng, R. Wang, C. Zhou, W. Xiong, Y. Yang, Chemosphere **222**, 184 (2019)
59. M.A. Espinoza-Sánchez, K. Arévalo-Niño, I. Quintero-Zapata, I. Castro-González, V. Almaguer-Cantú, J. Environ. Manag. **251**, 109595 (2019)
60. S. Haq, W. Rehman, M. Waseem, J. Inorg. Organomet. Polym. Mater. **29**, 651 (2019)
61. A.I.A. Sherlala, A.A.A. Raman, M.M. Bello, A. Buthiyappan, J. Environ. Manag. **246**, 547 (2019)
62. X.J. Gong, Y.S. Li, Y.Q. Dong, W.G. Li, Chemosphere **250**, 126275 (2020)
63. A. Nakarmi, S.E. Bourdo, L. Ruhl, S. Kanel, M. Nadagouda, P. Kumar Alla, I. Pavel, T. Viswanathan, J. Environ. Manag. **272**, 111048 (2020)
64. R. Bardestani, C. Roy, S. Kaliaguine, J. Environ. Manag. **240**, 404 (2019)
65. Z. Liu, X. He, X. Yang, H. Ding, D. Wang, D. Ma, Q. Feng, J. Mater. Sci. **56**, 11248 (2021)
66. B. Nayak, A. Samant, R. Patel, P.K. Misra, ACS Omega **2**, 8118 (2017)
67. A.A. Ali, I.S. Ahmed, E.M. Elfiky, J. Inorg. Organomet. Polym. Mater. **31**, 384 (2021)
68. J. Zhang, X. Ma, L. Yuan, D. Zhou, J. Environ. Manag. **256**, 109959 (2020)
69. Y. Su, J. Mater. Sci. **53**, 4078 (2018)
70. M. Rabiee Faradonbeh, A.A. Dadkhah, A. Rashidi, S. Tasharofi, F. Mansourkhani, J. Inorg. Organomet. Polym. Mater. **28**, 829 (2018)
71. B. Zhang, T. Zhang, Z. Zhang, M. Xie, J. Mater. Sci. **54**, 11037 (2019)
72. T. Ma, Y. Wu, N. Liu, Y. Wu, J. Inorg. Organomet. Polym. Mater. **30**, 4027 (2020)
73. A. Dąbrowski, Adv. Colloid Interface Sci. **93**, 135 (2001)
74. K. Vijayaraghavan, T.V.N. Padmesh, K. Palanivelu, M. Velan, J. Hazard. Mater. **133**, 304 (2006)
75. K.Y. Foo, B.H. Hameed, Chem. Eng. J. **156**, 2 (2010)
76. N.D. Hutson, R.T. Yang, Adsorption **3**, 189 (1997)
77. World Health Organization, Who/Sde/Wsh/03.04/08 **2**, 4 (2003)

Publisher's Note Springer Nature remains neutral with regard to jurisdictional claims in published maps and institutional affiliations.